

Topological Surface Transport in Epitaxial SnTe Thin Films Grown on Bi₂Te₃

A. A. Taskin,* Fan Yang, Satoshi Sasaki, Kouji Segawa, and Yoichi Ando[†]

Institute of Scientific and Industrial Research, Osaka University, Ibaraki, Osaka 567-0047, Japan

The topological crystalline insulator SnTe has been grown epitaxially on a Bi₂Te₃ buffer layer by molecular beam epitaxy. In a 30-nm-thick SnTe film, *p*- and *n*-type carriers are found to coexist, and Shubnikov–de Haas oscillation data suggest that the *n*-type carriers are Dirac fermions residing on the SnTe (111) surface. This transport observation of the topological surface state in a *p*-type topological crystalline insulator became possible due to a downward band bending on the free SnTe surface, which appears to be of intrinsic origin.

PACS numbers: 73.25.+i, 71.18.+y, 73.20.At, 72.20.My

The energy band inversion and time-reversal symmetry (TRS) are the main ingredients for realizing a nontrivial topology in Z_2 topological insulators (TIs) [1–4]. Recently, the family of TIs has been extended by the introduction of topological crystalline insulators [5, 6] where the topology is protected by a point-group symmetry of the crystal lattice rather than by TRS. The first material predicted to be a TCI was SnTe [6], in which the band inversion at an even number of time-reversal-invariant momenta (TRIMs) leads to a trivial Z_2 topological invariant, but its mirror symmetry gives rise to a nontrivial mirror Chern number $n_M = -2$ to guarantee the existence of topologically protected gapless surface states (SSs) on any surface containing a mirror plane. Angle-resolved photoemission spectroscopy (ARPES) experiments have confirmed the existence of Dirac-like SSs on the (001) surface of SnTe [7] and related compounds [8, 9], generating a lot of interest in TCIs [10, 11]. Naturally, an important next step is to elucidate the topological SSs with transport experiments, as was done for Z_2 TIs [12–21].

However, probing the SSs in SnTe by transport experiments is a challenge, because of a high concentration of bulk holes ($10^{20} - 10^{21} \text{ cm}^{-3}$) [22]. Nevertheless, in thin films, an enhanced surface-to-bulk ratio and a high surface mobility expected for topologically-protected SSs [23, 24] might make it possible to probe them in quantum oscillations. To obtain high-quality thin films by molecular beam epitaxy (MBE) [25–32], lattice matching of the substrate is crucial. In this regard, while BaF₂ is the usual choice of substrate for SnTe [33] with its $\sim 1.6\%$ lattice matching, we noticed that rhombohedral Bi₂Te₃ may be a better choice, at least for the (111) growth direction, with the lattice matching of $\sim 1.5\%$. Furthermore, the building block of Bi₂Te₃ is a Te-Bi-Te-Bi-Te quintuple layer (QL) terminated with a hexagonal Te plane, which naturally accommodates the Sn layer of the SnTe in the (111) plane [see Fig. 1(d)].

Here, we show that high-quality SnTe thin films can indeed be grown by MBE on Bi₂Te₃ and that they are actually suitable for probing the topological SSs in transport experiments. Those films present Shubnikov-de Haas (SdH) oscillations composed of two close frequen-

cies, whose dependence on the magnetic-field direction signifies that the observed oscillations stem from two-dimensional (2D) Fermi surfaces (FSs). Furthermore, the phase of the oscillations indicates that the 2D carriers are Dirac electrons bearing the Berry phase of π . Measurements of the *I*-*V* characteristics across the SnTe/Bi₂Te₃ interface and careful considerations of the energy-band diagram in this heterostructure lead us to conclude that the Dirac electrons reside on the top surface of SnTe.

The MBE growth was performed in an ultrahigh vacuum chamber with the base pressure better than 5×10^{-8} Pa. Before deposition of SnTe, a thin layer of high-quality Bi₂Te₃ was grown under Te-rich conditions on sapphire substrates [34] with a two-step deposition procedure similar to that used for Bi₂Se₃ films [27, 29, 35]. Both Bi (99.9999%) and Te (99.9999%) were evaporated from standard Knudsen cells. The Te₂(Te₄)/Bi flux ratio was kept at ~ 20 . The growth rate, which is determined by the Bi flux, was kept at 0.3 nm/min. After growing ~ 30 nm of the Bi₂Te₃ layer, Sn (99.999%) and Te were co-evaporated, keeping the Te₂(Te₄)/Sn flux ratio at ~ 40 , substrate temperature at 300°C, and the growth rate at 0.4 nm/min. The resistivity ρ_{xx} and the Hall resistivity ρ_{yx} of the films were measured in a Hall-bar geometry by a standard six-probe method on rectangular samples on which the contacts were made with silver paste or indium near the perimeter. The magnetic field was swept between ± 14 T at fixed temperatures.

A critical ingredient for the epitaxial SnTe growth in the present experiment is the high quality of the Bi₂Te₃ buffer layer. Figure 1(a) shows an atomic force microscopy (AFM) image of a 40-nm-thick Bi₂Te₃ thin film grown on sapphire substrate. Large equilateral triangles with atomically flat terraces, which have a height of exactly 1 QL, can be easily recognized. An AFM image of a 30-nm-thick SnTe film grown on top of such Bi₂Te₃ buffer layer is shown in Fig. 1(b). Triangles are still clearly seen on the surface, giving evidence for an epitaxial growth. The height of the terraces is ~ 0.4 nm, which agrees with the periodicity of the rock-salt lattice along the (111) direction [Fig. 1(d)]. (An image for a larger area with clear triangular morphology is shown in the

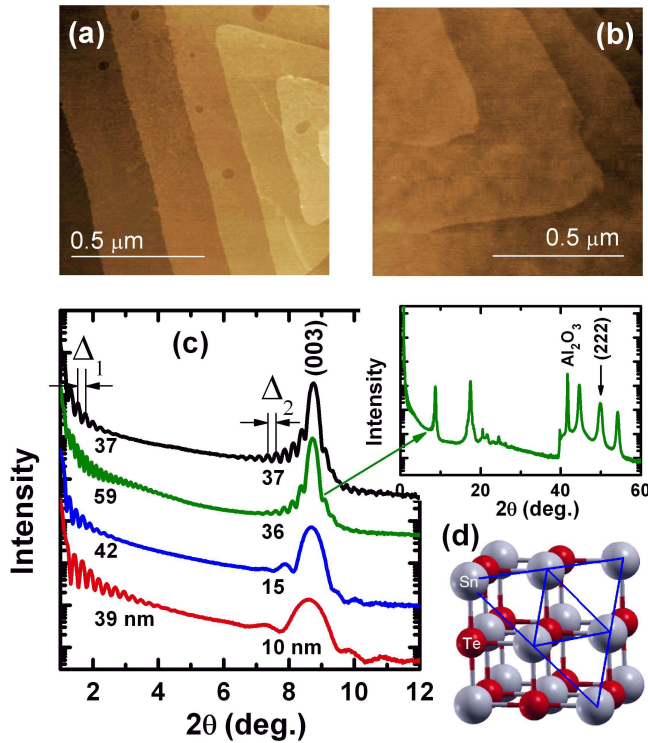


FIG. 1: (Color online) SnTe/Bi₂Te₃ heterostructure. (a) AFM image of the Bi₂Te₃ layer showing atomically flat terraces with 1-QL steps. (b) AFM image of the SnTe film grown on Bi₂Te₃ buffer layer. The step height of the terraces is ~ 0.4 nm. (c) Low-angle XRD patterns of a series of SnTe films grown on Bi₂Te₃ of different thickness. The total film thickness d_t given by the distance Δ_1 of Kiessig fringes at grazing angles is shown to the left. The fringe distance Δ_2 near the (003) Bi₂Te₃ Bragg peak gives the thickness of the Bi₂Te₃ layer, d_b , which is shown near the peak. The SnTe layer thickness is given by $d_t - d_b$. Inset shows a wide-angle XRD pattern. (d) The rocksalt lattice of SnTe with its (111) plane marked by triangles.

Supplemental Material (SM) [36]).

The high structural quality of both Bi₂Te₃ and SnTe films as well as the very smooth nature of the interface between them can be judged from the Kiessig fringes [36, 37] in the x-ray diffraction (XRD) measurements [Fig. 1(c); see also SM for more details]. The inset of Fig. 1(c) shows the XRD pattern for a wider angle range, in which SnTe only yields $(2n, 2n, 2n)$ Bragg peaks to confirm the (111) growth direction.

Figure 2(a) shows the temperature dependence of the resistivity, $\rho_{xx}(T)$, in a 30-nm-thick SnTe film grown on 36-nm-thick Bi₂Te₃. There is no discernible kink in the data, suggesting that the structural phase transition observed in bulk SnTe [22, 38, 39] is absent in our thin films and that the mirror symmetry is kept intact down to low temperature [36]. In the magnetotransport properties, a downward cusp observed in $\rho_{xx}(B)$ at very low fields [Fig. 2(b)] is a reflection of the weak antilocaliza-

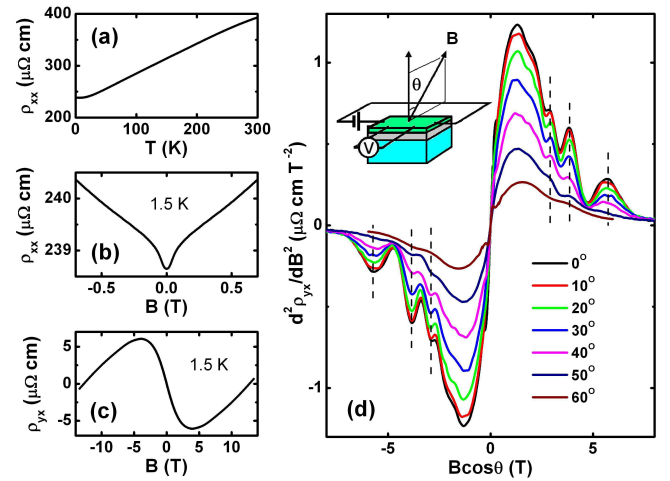


FIG. 2: (Color online) Transport properties of a 30-nm-thick SnTe film grown on a 36-nm Bi₂Te₃ buffer layer. (a) Temperature dependence of ρ_{xx} . (b) Low-field $\rho_{xx}(B)$ measured at 1.5 K. (c) $\rho_{yx}(B)$ measured at 1.5 K. (d) $d^2\rho_{yx}/dB^2$ at various angles are plotted vs $B \cos \theta$; inset shows the measurement geometry. Dashed lines mark the maxima in the oscillations.

tion behavior which is expected for topological materials [40–42]. We also observe a coexistence of n - and p -type carriers in the sample which is evident from a sign change of the slope in $\rho_{yx}(B)$ [Fig. 2(c)]. Importantly, we found that both $\rho_{yx}(B)$ and $\rho_{xx}(B)$ present SdH oscillations at high magnetic fields. To remove a large background and make the oscillations more visible, we employed second derivatives. Figure 2(d) shows $d^2\rho_{yx}/dB^2$ measured in tilted magnetic fields at 1.5 K and plotted as a function of $B \cos \theta$, where θ is the angle of the magnetic field from the surface normal. Since the maxima in the oscillations (marked by vertical dashed lines) appear at the same $B \cos \theta$ upon changing θ , the observed SdH oscillations clearly have a two-dimensional (2D) character. Note also that in our experiments, the SdH oscillations were not seen at tilting angles close to 90°, giving evidence against a three-dimensional (3D) FS as the origin of oscillations.

An important question is which of the n - or p -type carriers are responsible for the oscillations, and this can be answered in the following Landau-level (LL) index analysis. To properly construct the LL index plot, we use conductance G_{xx} and Hall conductance G_{xy} rather than ρ_{xx} and ρ_{yx} [4]. Figure 3(a) shows the plots of d^2G_{xx}/dB^2 and d^2G_{xy}/dB^2 vs $1/B$. The Fourier transform of d^2G_{xy}/dB^2 is shown in the inset of Fig 3(a). Its main feature is a broadened peak with a shoulder, which can be well fitted with two Gaussians centered at frequencies of 10.6 and 14 T. The coexistence of two branches of oscillations is actually anticipated from weak beating patterns in the data. The two frequencies $F_1 = 10.6$ T and $F_2 = 14$ T correspond to orbits on the FSs with radii of $k_F = 1.8 \times 10^6 \text{ cm}^{-1}$ and $2.1 \times 10^6 \text{ cm}^{-1}$, respectively.

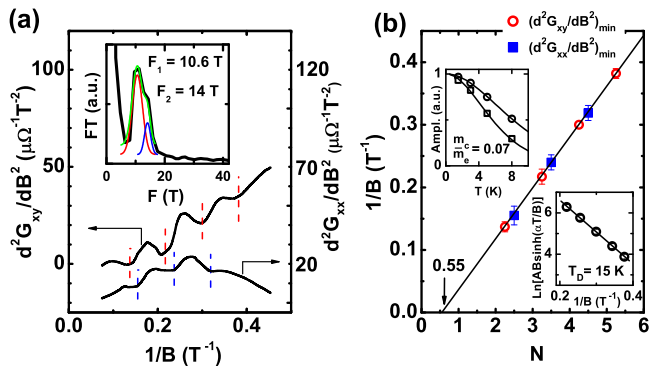


FIG. 3: (Color online) SdH oscillations. (a) d^2G_{xx}/dB^2 and d^2G_{xy}/dB^2 vs $1/B$ measured at $T = 1.5$ K and $\theta = 0^\circ$; inset shows the Fourier transform of the d^2G_{xy}/dB^2 oscillations revealing two close frequencies, 10.6 and 14 T (the upturn below ~ 5 T is related to the background which slowly changes with B). (b) LL index plot constructed from the minima in the oscillations of d^2G_{xx}/dB^2 and d^2G_{xy}/dB^2 . A half-integer index $N + \frac{1}{2}$ is assigned to a minimum in d^2G_{xx}/dB^2 . The index assignment for a minimum in d^2G_{xy}/dB^2 depends on the sign of the carriers: The index $N + \frac{1}{4}$ for electrons is consistent with the indices from G_{xx} , meaning that the SdH oscillations are produced by electrons. The solid line is a linear fitting to the data; its intercept of 0.55 on the N -index axis indicates the π Berry phase. Upper inset shows T dependencies of the SdH amplitudes measured at 2.67 T (squares) and 3.85 T (circles), both yielding $m_c = 0.07m_0$. Lower inset shows the Dingle plot for the data at 1.5 K, giving $T_D = 15$ K.

The corresponding 2D carrier densities n_s are 2.6×10^{11} cm^{-2} and 3.4×10^{11} cm^{-2} for each spin eigenvalue. Since the amplitude of the lower frequency oscillations is much larger than the amplitude of the higher frequency branch [see inset of Fig. 3(a)], the main contribution to the SdH oscillations is coming from the lower frequency branch; in such a case, the LL index plot constructed from weakly beating oscillations can still yield the correct phase factor for the lower frequency branch with reasonable accuracy (see SM for details). The constructed LL index plot [Fig. 3(b)] crosses the N -index axis at 0.55, which gives evidence for the Berry phase of π [43–45]. Also, the relative phase in the oscillations of d^2G_{xx}/dB^2 and d^2G_{xy}/dB^2 indicates that the carriers must be n -type (see SM for details). Therefore, the observed SdH oscillations can be concluded to be due to n -type 2D Dirac fermions bearing the π Berry phase. Note that, even though the Bi_2Te_3 layer contains a lot of n -type carriers (see SM), such carriers cannot be the source of the SdH oscillations, because the observed frequencies are an order of magnitude too low to represent the bulk FS of Bi_2Te_3 .

The temperature dependence of the SdH amplitude [upper inset of Fig. 3(b)] gives the cyclotron mass $m_c = 0.07m_0$ (m_0 is the free electron mass) [46]. This value should mainly reflect the lower frequency branch of oscillations ($F_1 = 10.6$ T) due to its dominance in the data,

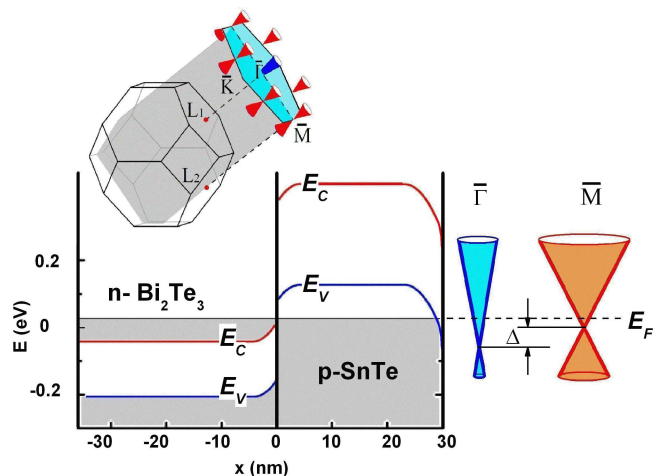


FIG. 4: (Color online) Energy-band diagram of $n\text{-Bi}_2\text{Te}_3/p\text{-SnTe}$ heterojunction. The broken-gap band lineup is concluded from the I - V characteristics of the heterojunction interface (see SM for details). Downward band-bending on the free surface of SnTe gives rise to n -type doping of surface Dirac cones shown schematically on the right. The upper inset shows the bulk Brillouin zone of SnTe and its projection along the (111) direction to the surface Brillouin zone, which hosts two kinds of Dirac cones at $\bar{\Gamma}$ and \bar{M} . The shaded plane is one of the three mirror planes $\{110\}$.

and we conclude that the upper limit of the Fermi velocity $v_F (= \hbar k_F/m_c)$ of the dominant surface carriers is about 3×10^7 cm/s. The Dingle analysis [lower inset of Fig. 3(b)] yields the Dingle temperature T_D of 15 K, from which the mean-free path of Dirac electrons $l^{\text{SdH}} = 24$ nm and their mobility $\mu_s^{\text{SdH}} = 2000$ cm^2/Vs are calculated [4]. Such a mobility is typical for best-quality SnTe films [33].

Now we discuss the origin of the observed n -type Dirac fermions. Both Bi_2Te_3 and SnTe have topological surface states, and it is useful to consider the energy-band diagram of the heterojunction (shown in Fig. 4) formed by degenerate p^+ -SnTe grown on the degenerate n^+ - Bi_2Te_3 . The lineup of the conduction and valence bands at the interface of two semiconductors is of fundamental importance for understanding the properties of the heterojunction. Essentially, there are three possibilities: straddling, staggered, and broken-gap band lineups [47] (see SM for details). The vast majority of heterojunctions have a straddling lineup with conduction- and valence-band offsets of opposite sign; in this case, when the two sides are doped with opposite types of carriers, an insulating barrier layer will be formed at the interface of such a $p-n$ junction. The same holds true for the case of a staggered lineup, in which conduction- and valence-band offsets have the same sign with a finite overlap of the gaps. The situation is different for the most exotic broken-gap lineup, in which the bottom of the conduction band of one semiconductor goes below the top of

the valence band of the other semiconductor as has been shown for InAs/GaSb heterostructures [48]. In this case, the system can behave as a semimetal without forming any barrier at the interface of a $p-n$ junction.

To determine which of the possible lineups is realized in our system, we measured $I-V$ curves across the interface in a sample where a part of the SnTe film has been etched away to make direct electrical contacts to both Bi₂Te₃ and SnTe layers (see SM). We found the $I-V$ characteristics to show Ohmic behavior, which led us to conclude that the SnTe/Bi₂Te₃ heterojunction most likely has the broken-gap lineup. In such a case, the Fermi level at the interface may lie above the bottom of the conduction band of Bi₂Te₃ and below the top of the valence band of SnTe. Hence, while some exotic 2D state may be formed at the Bi₂Te₃/SnTe interface [49–51], such a state is not accessible due to the position of the Fermi level and it is unlikely that the 2D SdH oscillations come from this interface.

Another interface between Bi₂Te₃ and sapphire is also an unlikely place for n -type Dirac fermions to reside on, because the Dirac point of the SS in Bi₂Te₃ is situated below the top of its valence band [52]. This means that, in order for the SdH oscillations with frequencies of only 10–14 T to be observed, a very large upward band bending sufficient for creating an inversion layer would be required at the interface with sapphire. This is very unlikely and, in fact, we have never observed such low-frequency SdH oscillations in Bi₂Te₃ films grown on sapphire.

Therefore, the only viable possibility is that the top SnTe surface has a sufficient downward band bending (Fig. 4) to host n -type Dirac fermions. Interestingly, such a band bending is naturally expected in materials with partially ionic bonding. For Sn²⁺Te²⁻ films grown in the [111] direction, the stacking sequence of atomic planes is Sn²⁺-Te²⁻..., which brings about a dipole moment and leads to a diverging electrostatic energy (see SM). This situation is known as the polar catastrophe [53] and cannot be realized in real materials; what actually happens is a partial charge compensation on the top and bottom surfaces to avoid the accumulation of electrostatic potential. In our system, the first atomic plane of the SnTe layer at the interface should be composed of Sn²⁺ and some of its positive charge is naturally compensated by n -type carriers of the Bi₂Te₃ layer. On the free surface side, the termination is either with Te²⁻ or Sn²⁺ planes; since the SnTe layer begins with Sn²⁺, the termination with Te²⁻ costs more electrostatic energy and Sn²⁺ termination is preferable (see SM). The resulting charge compensation leads to a downward band bending at the Sn²⁺-terminated free surface as shown in Fig. 4. This offers a natural explanation of the observed n -type carriers at the free SnTe surface. Note that a strong downward band bending is also observed in ARPES experiments [54] when p -type SnTe single crystals are cleaved along the [111] direction in vacuum.

The above picture allows us to consistently understand the measured transport data. On the (111) plane of SnTe which is a TCI, there are four Dirac cones centered at four TRIMs in the surface Brillouin zone (BZ) [54, 55]: one at $\bar{\Gamma}$ and three at \bar{M} points which are projections of the four L points in the 3D BZ along the [111] direction as schematically shown in the inset of Fig. 4. The surface band calculations give different results for Te and Sn terminations [55, 56]. For Te-terminated (111) surface, all Dirac points (DPs) touch the bottom of the conduction band, and it is impossible to realize n -type Dirac fermions irrespective of the position of the Fermi level. For the Sn-terminated (111) surface, on the other hand, the DPs are closer to the top of the valence band and Dirac electrons can be probed in transport experiments. Interestingly, epitaxially grown (111)-oriented films of a similar material, Pb_{1-x}Sn_xSe, were found to be preferentially terminated with Pb/Sn [57].

The observed two frequencies in the SdH oscillations are consistent with the existence of two types of Dirac cones on the free surface of SnTe reported in ARPES experiments [54]: the stronger, lower frequency branch is coming from electrons occupying the three Dirac cones at the \bar{M} points, while the weaker, higher frequency branch is coming from electrons occupying the sole Dirac cone at the $\bar{\Gamma}$ point. Importantly, the ARPES data show [54] that the Dirac point at $\bar{\Gamma}$ is lower in energy than that at \bar{M} , resulting in a higher Fermi energy for the Dirac cone at $\bar{\Gamma}$ (see Fig. 4) with a difference Δ of ~ 170 meV. It is worth noting that if oscillations were coming from the Bi₂Te₃ surface, there would be only one frequency. The same is true for the SnTe/Bi₂Te₃ interface, where the two Dirac cones at $\bar{\Gamma}$ originating from SnTe and Bi₂Te₃ should annihilate due to their opposite helicities [58]. The v_F of about 3×10^7 cm/s obtained from our data may be attributed to the averaged v_F of highly anisotropic DPs at \bar{M} [56]. From $F_1 = 10.6$ T ($k_F = 1.8 \times 10^6$ cm⁻¹), the position of the Fermi level above the DPs at \bar{M} is estimated to be about 40 meV. For the DP at $\bar{\Gamma}$, according to the ARPES data [54], the Fermi velocity is much larger, $v_F = 1.3 \times 10^7$ cm/s, and, for $F_2 = 14$ T ($k_F = 2.1 \times 10^6$ cm⁻¹), the position of the Fermi level would be about 180 meV above the DP. The energy difference of ~ 140 meV between the two types of Dirac cones obtained in our transport experiments is close to the ARPES result of $\Delta \sim 170$ meV, giving confidence that the observed 2D electrons indeed reside on the free surface of SnTe.

Finally, we mention that the observed SdH oscillations are prone to aging; namely, their amplitude was greatly reduced when we re-measured the sample after keeping it in nitrogen atmosphere for six months. This also supports the conclusion that the 2D oscillations are most likely coming from the free surface of SnTe. All in all, the present results demonstrate that the surface Dirac electrons residing on the (111) surface of SnTe can be accessed by transport measurements of high-quality films

grown on a Bi₂Te₃ buffer layer. These thin-film samples open new opportunities for experimentally exploring the physics of TCIs as well as for fabricating novel devices based on the unique nature of TCIs [59, 60].

We thank J. Liu and L. Fu for helpful discussions, and M. Kishi for technical assistance with micro-fabrication of samples for *I-V* measurements. This work was supported by JSPS (KAKENHI 24740237, 24540320, 25400328, and 25220708), MEXT (Innovative Area “Topological Quantum Phenomena” KAKENHI), and AFOSR (AOARD 124038).

* Electronic address: taskin@sanken.osaka-u.ac.jp

† Electronic address: y.ando@sanken.osaka-u.ac.jp

- [1] M.Z. Hasan and C.L. Kane, *Rev. Mod. Phys.* **82**, 3045 (2010).
- [2] J.E. Moore, *Nature (London)* **464**, 194 (2010).
- [3] X.-L. Qi and S.-C. Zhang, *Rev. Mod. Phys.* **83**, 1057 (2011).
- [4] Y. Ando, *J. Phys. Soc. Jpn.*, **82**, 102001 (2013).
- [5] L. Fu, *Phys. Rev. Lett.* **106**, 106802 (2011).
- [6] T. H. Hsieh, H. Lin, J. Liu, W. Duan, A. Bansil and L. Fu, *Nat. Commun.* **3**, 982 (2012).
- [7] Y. Tanaka, Z. Ren, T. Sato, K. Nakayama, S. Souma, T. Takahashi, K. Segawa, and Y. Ando, *Nat. Phys.* **8**, 800 (2012).
- [8] P. Dziawa, B. J. Kowalski, K. Dybko, R. Buczko, A. Szczerbakow, M. Szot, E. ?usakowska, T. Balasubramanian, B. M. Wojek, M. H. Berntsen *et al.*, *Nat. Mater.* **11**, 1023 (2012).
- [9] S.-Y. Xu, C. Liu, N. Alidoust, M. Neupane, D. Qian, I. Belopolski, J.D. Denlinger, Y.J. Wang, H. Lin *et al.*, *Nat. Commun.* **3**, 1192 (2012).
- [10] A. Gyenis, I. K. Drozdov, S. Nadj-Perge, O. B. Jeong, J. Seo, I. Pletikosić, T. Valla, G. D. Gu, and A. Yazdani, *Phys. Rev. B* **88**, 125414 (2013).
- [11] M. Safdar, Q. Wang, M. Mirza, Z. Wang, K. Xu, and J. He, *Nano Lett.* **13**, 5344 (2013).
- [12] A. A. Taskin and Y. Ando, *Phys. Rev. B* **80**, 085303 (2009).
- [13] A. A. Taskin, K. Segawa, and Y. Ando, *Phys. Rev. B* **82**, 121302(R) (2010).
- [14] D.-X. Qu, Y.S. Hor, J. Xiong, R.J. Cava, and N.P. Ong, *Science* **329**, 821 (2010).
- [15] J.G. Analytis, R.D. McDonald, S.C. Riggs, J.-H. Chu, G.S. Boebinger, and I.R. Fisher, *Nat. Phys.* **10**, 960 (2010).
- [16] Z. Ren, A. A. Taskin, S. Sasaki, K. Segawa, and Y. Ando, *Phys. Rev. B* **82**, 241306(R) (2010).
- [17] A. A. Taskin, Z. Ren, S. Sasaki, K. Segawa, and Y. Ando, *Phys. Rev. Lett.* **107**, 016801 (2011).
- [18] B. Sacépé, J. B. Oostinga, J. Li , A. Ubal dini, N. J. G. Couto, E. Giannini, and A. F. Morpurgo, *Nat. Commun.* **2**, 575 (2011).
- [19] S. S. Hong, J. J. Cha, D. Kong, and Y. Cui, *Nat. Commun.* **3**, 757 (2012).
- [20] L. He, F. Xiu, X. Yu, M. Teague, W. Jiang, Y. Fan, X. Kou, M. Lang, Y. Wang, G. Huang *et al.*, *Nano Lett.* **12**, 1486 (2012).
- [21] J. Xiong, Y. Luo, Y. H. Khoo, S. Jia, R. J. Cava, and N. P. Ong, *Phys. Rev. B* **86**, 045314 (2012).
- [22] R. Dornhaus, G. Nimtz, B. Schlicht, *Narrow-Gap Semiconductors* (Springer-Verlag, New York, 1983).
- [23] D. Culcer, E. H. Hwang, T. D. Stanescu, and S. Das Sarma, *Phys. Rev. B* **82**, 155457 (2010).
- [24] A. A. Taskin, S. Sasaki, K. Segawa, and Y. Ando, *Phys. Rev. Lett.* **109**, 066803 (2012).
- [25] G. Zhang, H. Qin, J. Teng, J. Guo, Q. Guo, X. Dai, Z. Fang, and K. Wua, *Appl. Phys. Lett.* **95**, 053114 (2009).
- [26] A. Richardella, D. M. Zhang, J. S. Lee, A. Koser, D. W. Rench, A. L. Yeats, B. B. Buckley, D. D. Awschalom, and N. Samarth, *Appl. Phys. Lett.* **97**, 262104 (2010).
- [27] H. D. Li, Z. Y. Wang, X. Kan, X. Guo, H. T. He, Z. Wang, J. N. Wang, T. L. Wong, N. Wang, and M. H. Xie, *New J. Phys.* **12**, 103038 (2010).
- [28] X. Chen, X.-C. Ma, K. He, J.-F. Jia, and Q.-K. Xue, *Adv. Mater.* **23**, 1162 (2011).
- [29] N. Bansal, Y. S. Kim, E. Edrey, M. Brahlek, Y. Horibe, K. Iida, M. Tanimura, G.-H. Li, T. Feng, H.-D. Lee *et al.*, *Thin Solid Films* **520**, 224 (2011).
- [30] N. Bansal, Y. S. Kim, M. Brahlek, E. Edrey, and S. Oh, *Phys. Rev. Lett.* **109**, 116804 (2012).
- [31] M. Lang, L. He, F. Xiu, X. Yu, J. Tang, Y. Wang, X. Kou, W. Jiang, A. V. Fedorov, and K. L. Wang, *ACS Nano* **6**, 295 (2012).
- [32] X. Yu, L. He, M. Lang, W. Jiang, F. Xiu, Z. Liao, Y. Wang, X. Kou, P. Zhang, J. Tang *et al.*, *Nanotechnology* **24**, 015705 (2013).
- [33] A. Ishida, T. Tsuchiya, T. Yamada, D. Cao, S. Takaoka, M. Rahim, F. Felder, and H. Zogg, *J. Appl. Phys.* **107**, 123708 (2010).
- [34] J. J. Lee, F. T. Schmitt, R. G. Moore, I. M. Vishik, Y. Ma, and Z. X. Shen, *Appl. Phys. Lett.* **101**, 013118 (2012).
- [35] A. A. Taskin, S. Sasaki, K. Segawa, and Y. Ando, *Adv. Mater.* **24**, 5581 (2012).
- [36] See Supplemental Material at (URL to be inserted) for supplemental data and discussion.
- [37] U. Pietsch, V. Holý, T. Baumbach, *High-Resolution X-Ray Scattering. From Thin Films to Lateral Nanostructures* (Springer, New York, 2004).
- [38] K. L. I. Kobayashi, Y. Kato, Y. Katayama, and K. F. Komatsubara, *Phys. Rev. Lett.* **37**, 772 (1976).
- [39] S. Katayama and D. L. Mills, *Phys. Rev. B* **22**, 336 (1980).
- [40] J. Chen, H. J. Qin, F. Yang, J. Liu, T. Guan, F. M. Qu, G. H. Zhang, J. R. Shi, X. C. Xie, C. L. Yang *et al.*, *Phys. Rev. Lett.* **105**, 176602 (2010).
- [41] J. Chen, X. Y. He, K. H. Wu, Z. Q. Ji, L. Lu, J. R. Shi, J. H. Smet, and Y. Q. Li, *Phys. Rev. B* **83**, 241304(R) (2011).
- [42] H. Steinberg, J. B. Lalöe, V. Fatemi, J. S. Moodera, and P. Jarillo-Herrero, *Phys. Rev. B* **84**, 233101 (2011).
- [43] A. A. Taskin and Y. Ando, *Phys. Rev. B* **84**, 035301 (2011).
- [44] G. P. Mikitik and Y. V. Sharlai, *Phys. Rev. B* **85**, 033301 (2012).
- [45] A. R. Wright and R. H. McKenzie, *Phys. Rev. B* **87**, 085411 (2013).
- [46] D. Shoenberg, *Magnetic Oscillations in Metals* (Cambridge University Press, Cambridge, 1984).
- [47] H. Kroemer, *Rev. Mod. Phys.* **73**, 783 (2001).
- [48] H. Sakaki, L. L. Chang, R. Ludeke, Chin-An Chang, G.

- A. Sai-Halasz, and L. Esaki Appl. Phys. Lett **31**, 211 (1977).
- [49] D. Soriano, F. Ortmann, and S. Roche, Phys. Rev. Lett. **109**, 266805 (2012).
- [50] S. Eremeev, G. Landolt, T. V. Menshchikova, B. Slomski, Y. M. Koroteev, Z. S. Aliev, M. B. Babanly, J. Henk, A. Ernst, L. Patthey *et al.*, Nat. Commun. **3**, 365 (2012).
- [51] M. Koleini, T. Frauenheim, and B. Yan, Phys. Rev. Lett. **110**, 016403 (2013).
- [52] Y.L. Chen, J. G. Analytis, J.-H. Chu, Z. K. Liu, S.-K. Mo, X. L. Qi, H. J. Zhang, D. H. Lu, X. Dai, Z. Fang, *et al.*, Science **325**, 178 (2009).
- [53] W. Weiss and W. Ranke, Prog. Surf. Sci. **70**, 1 (2002).
- [54] Y. Tanaka, T. Shoman, K. Nakayama, S. Souma, T. Sato, T. Takahashi, M. Novak, K. Segawa, and Y. Ando, Phys. Rev. B **88**, 235126 (2013).
- [55] J. Liu, W. Duan, and L. Fu, Phys. Rev. B **88**, 241303(R) (2013).
- [56] S. Safaei, P. Kacman, and R. Buczko, Phys. Rev. B **88**, 045305 (2013).
- [57] C. M. Polley, P. Dziawa, A. Reszka, A. Szczerbakow, R. Minikayev, J. Z. Domagala, S. Safaei, P. Kacman, R. Buczko, J. Adell *et al.*, arXiv:1312.3226.
- [58] T. Rauch, M. Flieger, J. Henk, and I. Mertig, Phys. Rev. B **88**, 245120 (2013).
- [59] J. Liu, T. H. Hsieh, P. Wei, W. Duan, J. Moodera, and L. Fu, Nat. Mater. **13**, 178 (2014).
- [60] C. Fang, M. J. Gilbert, and B. A. Bernevig, Phys. Rev. Lett. **112**, 046801 (2014).

Supplemental Material

S1. Resistivity behavior of Bi₂Te₃ buffer layer

Our Bi₂Te₃ films grown on sapphire substrates with MBE are always degenerately *n*-type doped. Figure S1 shows typical data of the temperature dependence of the resistivity ρ_{xx} . The bulk electron density n_b of this films is known from the Hall effect to be $4 \times 10^{19} \text{ cm}^{-3}$, from which one obtains the bulk mobility of about 400 and 100 cm²/Vs at 1.5 and 300 K, respectively.

S2. Kiessig fringes

Low-angle XRD patterns shown in Fig. 1c in the main text demonstrate clear Kiessig oscillations. Generally, such low-angle intensity oscillations are the result of x-ray interference between two interfaces of a thin film, indicating its homogeneity (uniform structure) and smoothness of the interfaces [35, 37]. The position of the *m*-th maximum θ_m in Kiessig fringes follows [37]

$$\theta_m^2 = \alpha_c^2 + m^2 \left(\frac{\lambda}{2t} \right)^2, \quad (1)$$

where α_c is the critical angle for the total external reflection, λ is the x-ray wavelength, and t is the thickness of a film. Since $\alpha_c \approx 0$ for x-rays, the film thickness can be accurately estimated as

$$t \approx \lambda/2\Delta, \quad (2)$$

where Δ is the period of Kiessig oscillations (i.e. fringe distance) in radian unit.

Our samples consist of sapphire (Al₂O₃) substrate, Bi₂Te₃ buffer layer, and SnTe layer; typical morphologies of Bi₂Te₃ and SnTe films over a large area of about $5 \times 5 \mu\text{m}^2$ are shown in Fig. S2. The fringe distance observed at grazing incidence angles reflects the total thickness d_t of the film, namely, the thickness of Bi₂Te₃ layer plus SnTe layer, and indeed, it exactly matches the thicknesses measured by AFM near a sharp edge. Interestingly, in our samples, Kiessig fringes are seen not only at grazing angles, but also near the (003) Bragg peak of Bi₂Te₃ layer. They have larger fringe distances which are the results of the interference within the Bi₂Te₃ buffer layer; hence, they testify to the high quality of both Al₂O₃/Bi₂Te₃ and Bi₂Te₃/SnTe interfaces and allow us to estimate the thickness d_b of the Bi₂Te₃ layer alone. [The top curve in Fig. 1c shows the data for Bi₂Te₃ film without deposition of SnTe, and hence the fringe distances at grazing angles and near the (003) peak are the same.] Since both d_t and d_b are known from those Kiessig fringes, the SnTe layer thickness is accurately estimated by calculating $d_t - d_b$.

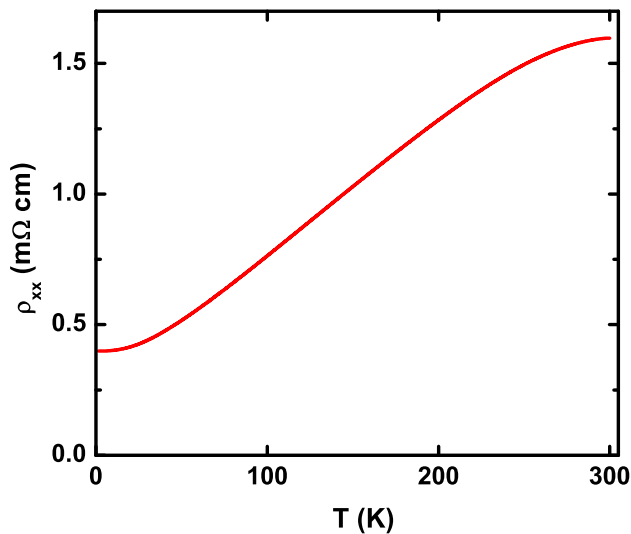


FIG. S1: Temperature dependence of ρ_{xx} of a 38-nm-thick Bi₂Te₃ film without SnTe deposition.

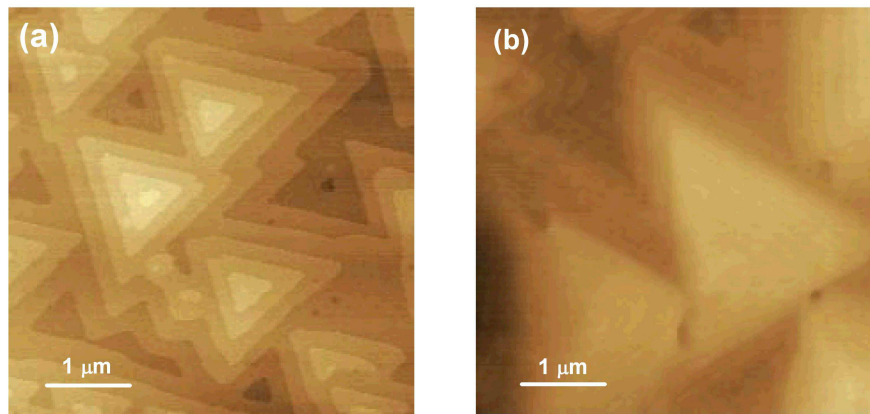


FIG. S2: AFM images of (a) 40-nm-thick Bi_2Te_3 film and (b) 40-nm-thick SnTe film on top of Bi_2Te_3 over a large area of about $5 \times 5 \mu\text{m}^2$.

S3. Ferroelectric transition in SnTe

SnTe is known to undergo a ferroelectric transition at low temperature, which is associated with a structural phase transition from cubic to rhombohedral [22, 38, 39]. In bulk single crystals, this ferroelectric transition manifests itself in the temperature dependence of ρ_{xx} as a kink [38]. In our thin films, however, the resistivity data do not present any feature ascribable to the ferroelectric transition, which suggests that the structural transition is suppressed by the epitaxial strain. The absence of the ferroelectric transition in strained films implies that the mirror symmetry is kept intact down to low temperature. Actually, even if the ferroelectric transition happens, it will *not* break the mirror symmetry on the surface of our films, because the structural distortion occurs along the [111] direction which is the same as the growth direction.

S4. Assignment of Landau-level indices

As discussed in detail in Ref. [4], for the assignment of Landau-level (LL) indices in the data of Shubnikov-de Haas (SdH) oscillations, the best practice is to start with the principle that an integer index N be assigned to a minimum in the conductance G_{xx} , and it follows that $N + \frac{1}{2}$ be assigned to a minimum in d^2G_{xx}/dB^2 . The index assignment for the Hall conductance G_{xy} depends on the sign of the carriers, and the correct assignment is most easily understood by considering the integer quantum Hall effect: For electrons, G_{xy} *increases* with B between the Hall plateaus and hence dG_{xy}/dB shows a *maximum* at $N + \frac{1}{2}$, whereas for holes G_{xy} *decreases* between plateaus to cause dG_{xy}/dB to show a *minimum* at $N + \frac{1}{2}$. Therefore, when the index assignment is to be done to a minimum in d^2G_{xy}/dB^2 , the index should be $N + \frac{1}{4}$ if the carriers are electrons, while it should be $N + \frac{3}{4}$ if they are holes. (Note that the LL index *decreases* with increasing B , which is the reason why a minimum in d^2G_{xy}/dB^2 should be at $N + \frac{1}{4}$ when a maximum in dG_{xy}/dB is at $N + \frac{1}{2}$.)

In the case of the data shown in Fig. 3 of the main text, it turns out that indices for electrons, $N + \frac{1}{4}$, should be assigned to the minima in d^2G_{xy}/dB^2 to make consistency with the indices from d^2G_{xx}/dB^2 , meaning that the SdH oscillations are produced by electrons.

S5. Landau-level index plot for weakly beating SdH oscillations

To understand the behavior of weakly beating SdH oscillations composed of two similar frequencies, let us consider a sum of two oscillating parts in the conductivity, $A_1 \cos\left(2\pi\frac{F}{B}\right)$ and $A_2 \cos\left(2\pi\frac{F+\delta}{B} + \alpha\right)$. In our data, $F = 10.6$ T and $\delta = 3.4$ T, and the amplitude A_1 is about three times larger than A_2 . The factor α is a possible phase shift between the two branches of oscillations. We simplify the calculations by setting the phase of the main branch to be 0. One can see that the sum of the two is also a cosine function, namely,

$$A_1 \cos\left(2\pi\frac{F}{B}\right) + A_2 \cos\left(2\pi\frac{F+\delta}{B} + \alpha\right) = A \cos\left(2\pi\frac{F}{B} + \phi\right), \quad (3)$$

where the amplitude A and the phase ϕ are given by

$$A = \sqrt{A_1^2 + A_2^2 + 2A_1A_2 \cos(2\pi \frac{\delta}{B} + \alpha)}, \quad (4)$$

$$\phi = \arctan \left[\frac{A_2 \sin(2\pi \frac{\delta}{B} + \alpha)}{A_1 + A_2 \cos(2\pi \frac{\delta}{B} + \alpha)} \right]. \quad (5)$$

The total amplitude A is not constant, but changes periodically between $A_1 - A_2$ and $A_1 + A_2$, which is the reason for beating. The new phase ϕ is also an oscillating function. From Eq. (5), it is easy to see that $|\phi|$ cannot exceed the value of $\arctan \frac{A_2}{A_1 - A_2}$, which is less than 0.15π for $A_1 : A_2 = 3 : 1$. This means that the phase of the weakly beating oscillations essentially follow the phase of the main branch (in our case, the lower-frequency component), and the deviation of the observed minima in G_{xx} from those of the main branch is at most 0.15π , which is smaller than the accuracy of our LL index analysis.

S6. Energy band lineups

A heterostructure is formed when a semiconductor is grown on top of another semiconductor. The lineups of the conduction and valence bands at the interface are of fundamental importance for engineering semiconductor devices [47, 61, 62]. Since the dawn of semiconductor technology, numerous models and theories have been developed for calculating the energy band offsets. One of the first attempts was the Anderson's electron affinity rule [63], which is based on the consideration of the energy balance for an electron moving from the vacuum energy level to the first semiconductor (gaining χ_1), then to the second semiconductor (losing ΔE_c), and then to the vacuum level again (losing χ_2). From the energy conservation, one obtains

$$\Delta E_c = \chi_1 - \chi_2, \quad (6)$$

where ΔE_c is the conduction-band offset and χ_1 (χ_2) is the electron affinity of the first (second) semiconductor. The valence-band offset follows automatically as

$$\Delta E_v = E_{g2} - E_{g1} - \Delta E_c, \quad (7)$$

where E_{g1} (E_{g2}) is the energy gap of the first (second) semiconductor. The electron affinity rule was successful in explaining the band discontinuities in many semiconductor heterostructures, but failed for some, which is due to the following limitations of this model [64]: First, it idealizes the surface of a semiconductor. In real crystals, the surface undergoes a reconstruction in order to reduce the surface energy. The rearrangement of atoms leads to the formation of a surface dipole layer which affects the electron affinity of a semiconductor. Surface defects and surface energy states also play roles. As a result, experimentally measured electron affinities are not very reliable. (This is actually the case with both SnTe and Bi₂Te₃, for which very different results have been reported in the literature [65–71].) Second, the surface reconstruction and surface energy states at the interface of two semiconductors are not necessarily the same as those on their free surfaces, making the energy balance consideration to be more complicated. Third, electron correlation effects also influence the electron affinity and have to be taken into consideration.

Over the years, there were many attempts to improve the description of the band offsets at interfaces. One of them is known as “common anion rule” [72–74] and deals with heterostructures which consist of semiconductors having a common anion element. This approach is based on the assumption that the valence band is mostly built from the atomic wave functions of anions, while the conduction band is mostly built from the atomic wave functions of cations. Therefore, the valence band of materials with the same anion element should be similar, implying that their valence-band offset in the heterostructure will be smaller than the conduction-band offset. This might seem appropriate to the SnTe/Bi₂Te₃ interface; however, the reality can be more complicated, especially in topological insulators where the *s*- and *p*-orbital characters of the wave functions forming the conduction and valence bands are interchanged in comparison with ordinary materials. A good example demonstrating such a band inversion is the (Sn_{1-x}Pb_x)Te system, in which a topological phase transition has been demonstrated in ARPES experiments [7].

Another approach to improve the simple electron affinity rule is the effective dipole model [75–77], which includes the effects of the dipole charge formation due to a local difference in the atomic (and electronic) structures at the interface in comparison with the bulk structures of constituent semiconductors.

Generally, there are only three possible band lineups [47] which are shown in Fig. S3. The straddling lineup with conduction- and valence-band offsets of opposite sign is the most common one. The staggered lineup has conduction- and valence-band offsets of the same sign. The broken-gap lineup is an extreme case of the staggered one, in which the

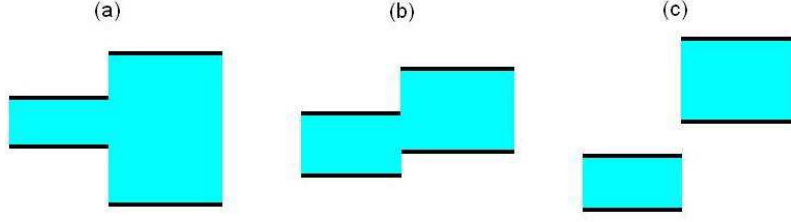


FIG. S3: Schematic picture of three possible types of band alignments: (a) straddling, (b) staggered, and (c) broken-gap band lineups.

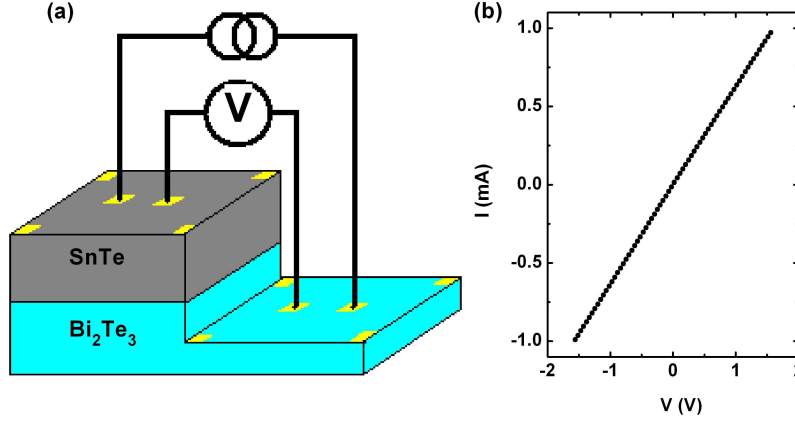


FIG. S4: (a) Schematic picture of the sample and the experimental setup for the $I - V$ measurements of the SnTe/Bi₂Te₃ interface. (b) The $I - V$ characteristics of a typical SnTe/Bi₂Te₃ junction.

bottom of the conduction band of one semiconductor goes below the top of the valence band of another semiconductor. This is the most exotic lineup and it is realized in at least one nearly-lattice-matched heterostructure, InAs/GaSb [48]. Another example, where the broken-gap lineup has been invoked to explain the coexistence of n - and p -type carriers, is the case of quantum-well structures and superlattices made of IV-VI semiconductors (such as PbTe/SnTe) for thermoelectric applications [69–71].

S7. The broken-gap lineup

To elucidate which of the three possible band lineups is realized in our p-SnTe/n-Bi₂Te₃ heterojunction, measurements of the $I - V$ characteristics with current flowing through the interface are useful. For both straddling and staggered lineups, an insulating barrier layer will be formed at the interface as a result of the p - n junction, while for the broken-gap lineup, the system behaves as a semimetal without any obstacles to the current at the interface. We therefore prepared samples for perpendicular $I - V$ measurements in the following way: First, rectangular-shaped islands were etched out from the SnTe/n-Bi₂Te₃ film. Second, one half of each island was slowly etched in the HCl:CH₃COOH:H₂O₂:H₂O solution in order to remove the SnTe layer and a part of the Bi₂Te₃ buffer layer as schematically shown in Fig. S4. Third, Pd contacts were deposited on top of both the SnTe and Bi₂Te₃ layers (Fig. S4a). The $I - V$ curves have been measured using a four-terminal dc-current method (Fig S4b). The resistivities of the SnTe/Bi₂Te₃-heterojunction part and the thinned-Bi₂Te₃-layer part of the islands have also been measured separately using the van der Pauw method. For all samples, we found linear $I - V$ characteristics with a negligible resistance of the interface (the total resistance is mostly coming from the thinned Bi₂Te₃ layer). Most likely, this result points to the realization of the broken-gap lineup in the SnTe/Bi₂Te₃ heterojunction.

S8. Te-termination vs Sn-termination

SnTe is a material with partially ionic bonding. For films grown in the [111] direction, the stacking sequence of atomic planes is Sn²⁺-Te²⁻-Sn²⁺-Te²⁻-... . Each uniformly charged atomic plane generates the electric field

$$E = \frac{\sigma}{2\epsilon\epsilon_0} \quad (8)$$

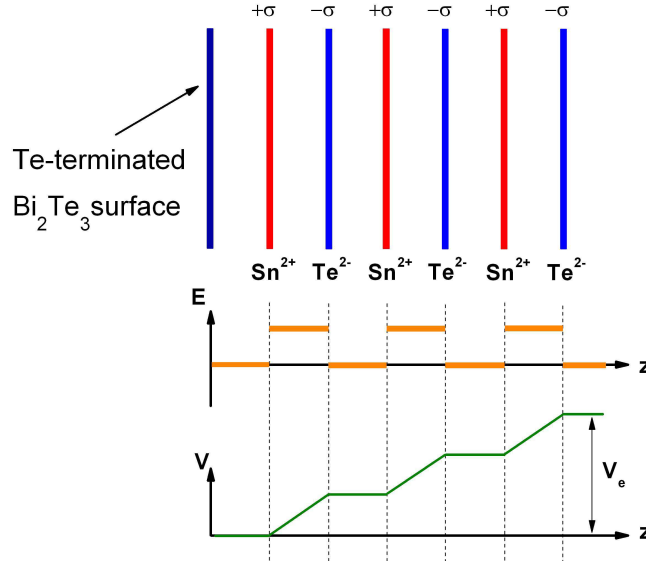


FIG. S5: The polar catastrophe. A schematic charge distribution in idealized ionic SnTe along the $[111]$ direction is shown together with the resulting variation of the electric field E and the electrostatic potential V along the $[111]$ direction denoted as z . Note the monotonic increase in V with increasing number of atomic planes.

where $+\sigma$ ($-\sigma$) is the charge density on the Sn^{2+} (Te^{2-}) plane, ϵ_0 is the permittivity of vacuum, and ϵ is the permittivity of SnTe. (Note that the charge density σ is expected to be small, because the bonding in SnTe is mostly covalent and is only partially ionic, due to the close electronegativity of Sn and Te.) Such a charge distribution brings about a finite electric field between each pair of Sn^{2+} and Te^{2-} planes, and, hence, a monotonic increase in the electrostatic energy as shown in Fig. S5. For increasing number of atomic layers along the polar direction, the electrostatic energy diverges. This situation is known as a polar catastrophe and cannot be realized in real materials [53]. One way to avoid the polar catastrophe is to partially compensate the charge on the surfaces of SnTe with mobile carriers as shown in Figs. S6 and S7.

In our system, the SnTe layer starts with a Sn^{2+} atomic plane, which should be compensated with a negative charge. This is naturally realized due to easily available electrons in the n -type Bi_2Te_3 buffer layer. If the free surface is terminated with Te, the negative charge of the outermost Te^{2-} plane must be compensated by positive charge (Fig. S6). The charge compensation makes E to change between positive and negative values along z , and the resulting profile of V just oscillates between zero and a finite positive value. Nevertheless, in this Te-terminated case, there remains a finite electrostatic potential V_e at the outer surface (Fig. S6).

On the other hand, if the free surface is terminated with Sn, the positive charge of the outermost Sn^{2+} plane must be compensated by negative charge (Fig. S7). In this case of the charge-compensated Sn-terminated surface, the remaining electrostatic potential can be exactly zero (Fig. S7). Compared with a finite V_e in the case of Te-terminated surface (Fig S6), the Sn-termination results in lower electrostatic energy and thus is energetically favored. This means that our films are more likely terminated with a Sn^{2+} atomic plane.

We note that our transport data points to the existence of a small density of high-mobility n -type carriers in the heterostructure, which is only possible when the outer surface has a downward band bending to cause the topological surface state to be doped with n -type carriers. Such a band bending is actually expected for the Sn-terminated surface which is compensated with negative charge, but the Te-terminated surface will have an upward band-bending due to its compensation with positive charge. Therefore, the conclusion about the termination based on the electrostatic energy argument is supported by the transport results.

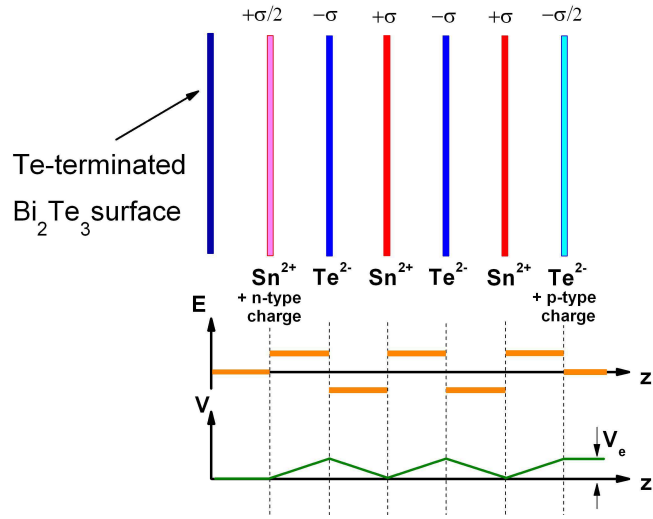


FIG. S6: The situation for Te-terminated SnTe film with charge compensation. A finite electrostatic potential V_e remains at the outer surface.

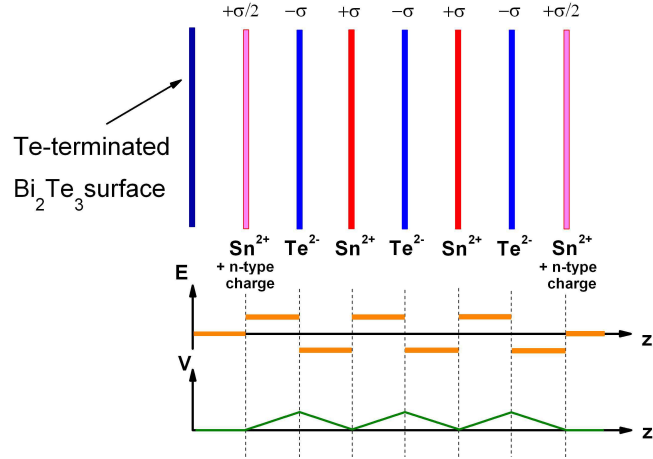


FIG. S7: The situation for Sn-terminated SnTe film with charge compensation. Remaining electrostatic potential V_e is zero.

* Electronic address: taskin@sanken.osaka-u.ac.jp

† Electronic address: y'ando@sanken.osaka-u.ac.jp

- [61] Z. I. Alferov, Rev. Mod. Phys. **73**, 767 (2001).
- [62] C. G. de Walle and J. N. Neugebauer, Nature **423**, 626 (2003).
- [63] R. L. Anderson, Solid-St. Electron. **5**, 341 (1962).
- [64] H. Kroemer, *Molecular Beam Epitaxy and Heterostructures*, edited by L. L. Chang and K. Ploog (NATO ASI Series, Martinus Nijhoff, 1985).
- [65] D. Haneman, J. Phys. Chem. Solids **11**, 205 (1959).
- [66] L.P. Bulat, D. Kossakovski, D.A. Pshenay-Severin, arXiv:1209.4492.
- [67] P. J. Stile, J de Physique, **29**, C4-105 (1968).
- [68] K. Koike, R. Kawaguchi, and M. Yano, Physica E **42**, 2636 (2010).
- [69] A. Ishida, M. Aoki, and H. Fujiyasu J. Appl. Phys. **58**, 1901 (1985).
- [70] E. I. Rogacheva, O. N. Nashchekina, A. V. Meriuts, S. G. Lyubchenko, M. S. Dresselhaus and G. Dresselhaus, Appl. Phys. Lett **86**, 063103 (2005).
- [71] A. Ishida, T. Yamada, T. Tsuchiya, Y. Inoue, S. Takaoka, and T. Kita Appl. Phys. Lett **95**, 122106 (2009).
- [72] J. O. McCaldin, T. C. McGill, and C. A. Mead, Phys. Rev. Lett. **36**, 56 (1976).
- [73] W. R. Frensley and H. Kroemer, Phys. Rev. B **16**, 2642 (1977).
- [74] S. P. Kowalczyk, W. J. Schaffer, E. A. Kraut, and R. W. Grant J. Vac. Sci. Technol. **20**, 705 (1982).
- [75] J. Tersoff, J. Vac. Sci. Technol. **B4**, 1066 (1986).
- [76] W. A. Harrison and J. Tersoff, J. Vac. Sci. Technol. **B4**, 1068 (1986).
- [77] Y.-C. Ruan and W. Y. Ching, J. Appl. Phys. **62**, 2885 (1987).